

---

# ADAPTIVE FINITE ELEMENT METHOD FOR PHASE FIELD FRACTURE MODELS BASED ON RECOVERY ERROR ESTIMATES

---

• **Tian Tian**

School of Mathematics and Computational Science  
Xiangtan University  
China, Xiangtan 411105  
tiantian@smail.xtu.edu.cn

• **Chen Chunyu**

School of Mathematics and Computational Science  
Xiangtan University  
China, Xiangtan 411105  
cbtxs@smail.xtu.edu.cn

• **He Liang**

School of Mathematics and Computational Science  
Xiangtan University  
China, Xiangtan 411105  
lianghesmail@163.com

• **Wei Huayi**\*

School of Mathematics and Computational Science, Xiangtan University  
National Center of Applied Mathematics in Hunan  
Hunan Key Laboratory for Computation and Simulation in Science and Engineering  
China, Xiangtan 411105  
weihuayi@xtu.edu.cn

October 3, 2024

## ABSTRACT

The phase field model is a widely used mathematical approach for describing crack propagation in continuum damage fractures. In the context of phase field fracture simulations, adaptive finite element methods (AFEM) are often employed to address the mesh size dependency of the model. However, existing AFEM approaches for this application frequently rely on heuristic adjustments and empirical parameters for mesh refinement. In this paper, we introduce an adaptive finite element method based on a recovery type posteriori error estimates approach grounded in theoretical analysis. This method transforms the gradient of the numerical solution into a smoother function space, using the difference between the recovered gradient and the original numerical gradient as an error indicator for adaptive mesh refinement. This enables the automatic capture of crack propagation directions without the need for empirical parameters. We have implemented this adaptive method for the Hybrid formulation of the phase field model using the open-source software package FEALPy. The accuracy and efficiency of the proposed approach are demonstrated through simulations of classical 2D and 3D brittle fracture examples, validating the robustness and effectiveness of our implementation.

**Keywords** Damage fracture · Phase field model · Finite element method · Recovery type posterior error estimates · Adaptive refinement

## 1 Introduction

The study of continuous material damage and fracture phenomena holds immense significance in the realm of materials science and engineering. These phenomena, influenced by factors such as external loads, thermal stress, and chemical

---

\*Corresponding author.

reactions, can profoundly impact the performance of components and structures, potentially leading to catastrophic fracture incidents [1]. Understanding and predicting crack propagation mechanisms is therefore crucial for enhancing the reliability and durability of materials and structures across diverse engineering sectors, including aerospace, automotive, construction, and energy [2, 3, 4].

The generation of cracks is often accompanied by discontinuities. Addressing these discontinuities presents significant computational challenges[5, 6]. The phase field model is used to describe this problem due to its unique advantages[39, 40]. The phase field model describes cracks by introducing continuous phase field variables, avoiding singularity problems in traditional fracture mechanics and effectively simulating complex crack paths. It does not require special treatment of the crack and can directly transform the crack equation into a simple diffusion equation. It assumes that the surface tension of the crack naturally exists. It can easily handle topological changes such as squeezing or merging cracks and is also easy to combine with various physical equations [39, 15, 16, 20]. The phase field model can fully consider the microstructure and damage evolution of materials, thus providing a more accurate description of material behavior.

Bourdin[14] proposed a linear elastic isotropic phase field model in 2000, wherein both displacement and phase field are treated as linear problem. Amor [12] introduced a method based on volume-biased strain decomposition in 2009, which breaks down the total elastic strain energy into volume and deviation contributions to suppress crack propagation under compression. Miehe[10, 11] proposed a spectral decomposition method in 2010 based on crack surface density energy, facilitating the separation of tension and compression effects on crack generation and preventing unrealistic cracks under compression. To reduce algorithmic complexity, Ambati[13] introduced a new approach in 2015. This approach involved a mixed phase field formulation. The formulation combined Bourdin’s linear elastic isotropic phase field model with Miehe’s maximum historical strain field function. This combination helped enhance computational efficiency. Additionally, it prevented crack reversibility and spurious cracks under compression.

Given the critical role of mesh size in phase field model, especially in fracture simulation, wherein mesh points at the crack tip must be sufficiently small, adaptive mesh refinement becomes indispensable. In 1978, Babuska[17, 18, 19] proposed the adaptive finite element method. This method can be applied to areas of interest, and numerical simulations can be performed at a lower cost. In previous studies of fracture phase field model, many scholars have proposed different adaptive strategies to determine mesh refinement regions during fracture evolution[34, 35, 36]. Yue et al.[30] utilized local error estimators based on gradients of the phase-field variable and mechanical fields to mark elements for refinement, capturing tensile, compressive, and shear fractures with high precision. Tian et al.[31] combined error estimation with heuristic marking rules to track changes in the phase-field and stress fields, making the approach suitable for both quasi-static and dynamic fracture scenarios. Krishnan et al.[32] developed a method that integrates error estimators with phase-field evolution, marking elements with rapid phase-field changes for refinement and coarsening those far from the fracture front to enhance computational efficiency. Assaf et al.[33] adopted an octree-based adaptive method, marking elements for refinement based on local stress-strain gradients, showing promising results in simulating 3D brittle fractures.

In this paper, we propose an adaptive finite element method grounded in recovery type posterior error estimates. This method employs either the average or the least squares approach to recovery the gradient of the numerical solution of the phase field from a piecewise constant space to a smoother, piecewise continuous function space[44, 45, 46, 43]. The disparity between the smoothed and original numerical solutions serves as an error estimate for adaptive refinement of mesh elements [38]. Compared to the traditional adaptive mesh refinement methods used in phase-field fracture models, the recovery-type posterior error estimation approach offers significant advantages. Rather than simply relying on phase-field values, gradients, or stress-strain variations, it directly evaluates errors through higher-order approximations based on the concept of error equidistribution, allowing for precise capture of crack details and automatic identification of refinement regions, eliminating the need for predefined thresholds. Additionally, recovery-type posterior error estimation is independent of the specific problem or finite element method, making it easy to implement with low computational cost and high robustness, especially in large-scale 3D fracture simulations.

We leverage the open-source numerical PDE solver FEALPy[37], utilizing object-oriented and array-based programming techniques to efficiently implement the proposed algorithms. FEALPy is developed entirely using standard Python scientific computing libraries, such as NumPy [56], SciPy [57], and Matplotlib [58], and provides a rich set of mesh data structures and adaptive algorithms, including commonly used 1D, 2D, and 3D mesh objects, as well as refinement methods like bisection and red-green refinement. Our implementation employs array-based programming to maintain code simplicity while ensuring high computational efficiency. Additionally, we introduce matrix assembly techniques that avoid numerical integration, and GPU acceleration to solve the discrete systems, significantly enhancing algorithm performance. Numerous classical examples are presented to validate the efficiency of our implementation.

The remainder of this paper is organized as follows. In section 2, we introduce the energy function, control equations of the fracture phase field model, and the formulation phase field model. In section 3, we introduce the algorithm used in

this article, including the adaptive finite element method, posterior error estimates, and the corresponding program algorithm flow. In section 4, we present the numerical experimental results of several classic examples. In section 5, we have summarized the the contributions and findings of this study.

## 2 Mathematical model

### 2.1 Crack energy function

Given a material region  $\Omega$ , if we apply a force  $\mathbf{f}$ , it will lead to deformation of the material. This deformation can be measured by displacement  $\mathbf{u}$ . If cracks occur during this deformation process, the material can be classified into two states, and we can use phase function  $d$  to describe them: cracked ( $d = 1$ ) and uncracked ( $d = 0$ )[38, 22]. At this point, fracture energy density function can be expressed as

$$\gamma(d, \nabla d) = \frac{1}{c_h} \left( \frac{h(d)}{l_0} + l_0 |\nabla d|^2 \right) \quad (1)$$

- $l_0 > 0$ : a small regularization length scale parameter [38, 8, 9], used to control the width of the smoothly approximated crack.
- $h(d)$ : a continuously and strictly increasing function.
- Normalization constant  $c_h = \int_0^1 \sqrt{h(\bar{d})}$ : a constant related to  $h(d)$  that ensures the regularization crack surface converges to the shaped crack surface as  $l_0 \rightarrow 0$ .

There are generally two options for fracture energy density function, namely:

- AT1 model:  $h(d) = d, c_h = \frac{8}{3}$  (finite width damage band, including pure elastic stage)
- AT2 model:  $h(d) = d^2, c_h = 2$  (infinite width damage band)

In this article, we use the AT2 model. The formulation presented here is based on the format proposed by Miehe[10, 11] et al. The expressions for fracture energy  $E_c(d)$  are defined as follows:

$$E_c(d) = G_c \int_{\Omega} \gamma(d, \nabla d) d\mathbf{x} \quad (2)$$

Here,  $G_c > 0$  denotes the critical energy release rate of the material[7].

### 2.2 Strain energy function with crack propagation

The energy stored by materials under external forces is called strain energy. For elastic materials, when external forces are eliminated, this energy will be completely released. However, in the case of crack propagation during the deformation process, a portion of the stored strain energy will be lost. Therefore, it is necessary to introduce the energy degradation function  $g(d)$  in the expression of strain energy to consider crack propagation. The energy degradation function is defined as

$$g(d) = (1 - d)^2 + \epsilon, \quad (3)$$

where  $0 \leq \epsilon \ll 1$  is introduced to ensure numerical stability. Of course, the energy degradation function can also choose other formats[23, 24, 25, 21]. At this point, strain energy is expressed as

$$E_s(\mathbf{u}, d) = \int_{\Omega} g(d) e_s(\boldsymbol{\varepsilon}) d\mathbf{x} - W(\mathbf{u}), \quad (4)$$

where,  $W(\mathbf{u})$  is the external force. The strain tensor  $\boldsymbol{\varepsilon}$  is given by:

$$\boldsymbol{\varepsilon} = \frac{1}{2} (\mathbf{u} \otimes \nabla + \nabla \otimes \mathbf{u}). \quad (5)$$

However, the above expression does not distinguish between tensile and compressive stress states, and spurious cracks may form in regions under compression. To avoid this situation, the commonly used processing method involves dividing the energy density  $e_s(\boldsymbol{\varepsilon})$  is divided into positive (related to tension state) and negative (compression state) parts, and applying the degradation function only to the positive component. This results in the following expression:

$$E_s(\mathbf{u}, d) = \int_{\Omega} [g(d) e_s^+(\boldsymbol{\varepsilon}) + e_s^-(\boldsymbol{\varepsilon})] d\mathbf{x} - W(\mathbf{u}). \quad (6)$$

### 2.3 Governing equations

According to the previous energy formula, we can obtain the total potential energy function:

$$\begin{aligned} L &= K(\dot{\mathbf{u}}) - \Pi(\mathbf{u}, d) \\ &= \frac{1}{2} \int_{\Omega} \rho \dot{\mathbf{u}} \cdot \dot{\mathbf{u}} \, dx - \Pi(\mathbf{u}, d), \end{aligned} \quad (7)$$

where

$$\begin{aligned} \Pi(\mathbf{u}, d) &= E_s(\mathbf{u}, d) + E_c(d) \\ &= \int_{\Omega} [(1-d)^2 + \epsilon] e_s^+(\boldsymbol{\varepsilon}) + e_s^-(\boldsymbol{\varepsilon}) \, dx \\ &\quad + \int_{\Omega} \frac{G_c}{2} \left[ \frac{1}{l_0} d^2 + l_0 |\nabla d|^2 \right] \, dx - \int_{\Omega} \mathbf{f} \cdot \mathbf{u} \, dx. \end{aligned} \quad (8)$$

According to the Hamiltonian principle, the variation of the Lagrange operator can lead to the Euler Lagrange equation:

$$\begin{cases} \rho \ddot{\mathbf{u}} - \operatorname{div} \boldsymbol{\sigma} = \mathbf{f} \\ g'(d) e_s^+(\boldsymbol{\varepsilon}) + G_c \gamma'(d, \nabla d) = 0. \end{cases} \quad (9)$$

The stress tensor  $\boldsymbol{\sigma}$  is:

$$\boldsymbol{\sigma}(\boldsymbol{\varepsilon}) := g(d) \frac{\partial e_s^+(\boldsymbol{\varepsilon})}{\partial \boldsymbol{\varepsilon}} + \frac{\partial e_s^-(\boldsymbol{\varepsilon})}{\partial \boldsymbol{\varepsilon}}. \quad (10)$$

### 2.4 Hybrid phase field model

For the "Isotropic" Model [14], strain energy density decomposition is defined as:

$$e_s^+(\boldsymbol{\varepsilon}) = e_s(\boldsymbol{\varepsilon}), \quad e_s^-(\boldsymbol{\varepsilon}) = 0. \quad (11)$$

Here, the strain energy density of linear isotropic materials is defined as:

$$e_s = \frac{\lambda}{2} \operatorname{tr}(\boldsymbol{\varepsilon})^2 + \mu \boldsymbol{\varepsilon} : \boldsymbol{\varepsilon}. \quad (12)$$

Where,  $\lambda$  is the Lamé's first parameter,  $\mu$  is the Lamé's second parameter (shear modulus), and  $\mu > 0$ ,  $\lambda + 2\mu > 0$ . Their relationships with Young's modulus  $E$ , Poisson's ratio  $\nu$  are as follows:

$$\lambda = \frac{\nu E}{(1 + \nu)(1 - 2\nu)}, \quad \mu = \frac{E}{2(1 + \nu)}. \quad (13)$$

Miehe [10, 11] proposed a spectral decomposition method, where strain energy density decomposition is defined as:

$$\begin{cases} e_s^+(\boldsymbol{\varepsilon}) &= \frac{\lambda}{2} \langle \operatorname{tr}(\boldsymbol{\varepsilon}) \rangle_+^2 + \mu \operatorname{tr}(\boldsymbol{\varepsilon}_+^2) \\ e_s^-(\boldsymbol{\varepsilon}) &= \frac{\lambda}{2} \langle \operatorname{tr}(\boldsymbol{\varepsilon}) \rangle_-^2 + \mu \operatorname{tr}(\boldsymbol{\varepsilon}_-^2), \end{cases} \quad (14)$$

and,

$$\boldsymbol{\varepsilon}_{\pm} = \sum_{i=0}^{n-1} \langle \varepsilon_i \rangle_{\pm} \mathbf{n}_i \otimes \mathbf{n}_i, \quad (15)$$

where,

- $\varepsilon_i$  represents eigenvalues.
- $\mathbf{n}_i \otimes \mathbf{n}_i$  represents eigenvectors.
- $\langle \cdot \rangle_{\pm}$  is Macqualay operation, which is defined as:  $\langle x \rangle_{\pm} = \frac{1}{2}(x \pm |x|)$ .

As crack growth is an irreversible phenomenon, Miehe proposed a maximum strain field function:

$$\mathcal{H}(\mathbf{x}, t) = \max_{s \in [0, t]} e_s^+(\boldsymbol{\varepsilon}(\mathbf{x}, s)) \quad (16)$$

to replace  $e_s^+(\boldsymbol{\varepsilon})$  in the equation  $g'(d) e_s^+(\boldsymbol{\varepsilon}) + G_c \gamma'(d, \nabla d) = 0$ , which can prevent the occurrence of non-physical crack closure.

In the hybrid mixed format [13], the "Isotropic" model is combined with Miehe's [10] maximum historical strain field function to obtain a linear mixed model, where the expression for the stress tensor is

$$\boldsymbol{\sigma}(\boldsymbol{\varepsilon}) = g(d) \frac{\partial e_s(\boldsymbol{\varepsilon})}{\partial \boldsymbol{\varepsilon}} = g(d) [\lambda(\text{tr}(\boldsymbol{\varepsilon})\mathbf{I}) + 2\mu\boldsymbol{\varepsilon}]. \quad (17)$$

And the fourth-order elastic tangent operator tensor:

$$\mathbb{C} := \frac{\partial \boldsymbol{\sigma}}{\partial \boldsymbol{\varepsilon}} = g(d) (\lambda \mathbf{I} \otimes \mathbf{I} + 2\mu \mathbb{I}). \quad (18)$$

Therefore, the final governing equations become:

$$\begin{cases} \rho \ddot{\mathbf{u}} - \text{div} \boldsymbol{\sigma} = \mathbf{f} \\ g'(d) \mathcal{H} + G_c \gamma'(d, \nabla d) = 0, \end{cases} \quad (19)$$

with

$$\begin{cases} d = 0, \text{ on } \partial\Omega \\ \boldsymbol{\sigma} \cdot \mathbf{n} = \mathbf{g}, \text{ on } \Gamma_N. \end{cases} \quad (20)$$

### 3 Algorithm design

#### 3.1 Nonlinear finite element discretization

In this article, we only consider quasi-static fracture, so we can abandon term  $\rho \ddot{\mathbf{u}}$ . Using the finite element method, the variational formulation of the governing equations can be derived, yielding the weak form as follows:

$$\begin{cases} (\boldsymbol{\sigma}(\mathbf{u}), \boldsymbol{\varepsilon}(\mathbf{v}))_{\Omega} = (\mathbf{f}, \mathbf{v})_{\Omega} + \langle \mathbf{g}, \mathbf{v} \rangle_{\Gamma_N}, & \mathbf{v} \in (H^1)^{\dim}(\Omega) \\ -2((1-d)\mathcal{H}, \omega)_{\Omega} + G_c l_0 (\nabla d, \nabla \omega)_{\Omega} + \frac{G_c}{l_0} (d, \omega)_{\Omega} = 0, & \omega \in H^1(\Omega), \end{cases} \quad (21)$$

where,  $\dim$  is the dimension of the problem.

In this article, we use triangle and tetrahedral mesh for discretization. We discretize  $H^1(\Omega)$  by finite element space, and the maximum strain field  $\mathcal{H} \in L^2(\Omega)$ . The discretization weak form is:

$$\begin{cases} (\boldsymbol{\sigma}(\mathbf{u}_h), \boldsymbol{\varepsilon}(\mathbf{v}_h))_{\Omega} = (\mathbf{f}, \mathbf{v}_h)_{\Omega} + \langle \mathbf{g}, \mathbf{v}_h \rangle_{\Gamma_N} \\ -2((1-d_h)\mathcal{H}, \omega_h)_{\Omega} + G_c l_0 (\nabla d_h, \nabla \omega_h)_{\Omega} + \frac{G_c}{l_0} (d_h, \omega_h)_{\Omega} = 0. \end{cases} \quad (22)$$

Let the basis functions for the Lagrange scalar space be denoted as  $\phi$ , and the basis functions for the Lagrange vector space be denoted as  $\Phi$ . At this point, the discretization weak form can be obtained:

$$\begin{cases} (\boldsymbol{\sigma}(\mathbf{u}_h), \boldsymbol{\varepsilon}(\Phi))_{\Omega} = (\mathbf{f}, \Phi)_{\Omega} + \langle \mathbf{g}, \Phi \rangle_{\Gamma_N} \\ -2((1-d_h)\mathcal{H}, \phi)_{\Omega} + G_c l_0 (\nabla d_h, \nabla \phi)_{\Omega} + \frac{G_c}{l_0} (d_h, \phi)_{\Omega} = 0. \end{cases} \quad (23)$$

The residual vectors  $\mathbf{R}_0$  and  $\mathbf{R}_1$  are defined as:

$$\begin{aligned} \mathbf{R}_0 &= (\mathbf{f}, \Phi)_{\Omega} + \langle \mathbf{g}, \Phi \rangle_{\Gamma_N} - (\boldsymbol{\sigma}(\mathbf{u}_h), \boldsymbol{\varepsilon}(\Phi))_{\Omega} \\ \mathbf{R}_1 &= 2((1-d_h)\mathcal{H}(\mathbf{u}_h), \phi)_{\Omega} - G_c l_0 (\nabla d_h, \nabla \phi)_{\Omega} - \frac{G_c}{l_0} (d_h, \phi)_{\Omega}. \end{aligned} \quad (24)$$

We employ the Newton-Raphson method for iterative solving, which leads to the following system of equations:

$$\begin{bmatrix} -\frac{\partial \mathbf{R}_0}{\partial \mathbf{u}_h} & -\frac{\partial \mathbf{R}_0}{\partial d_h} \\ -\frac{\partial \mathbf{R}_1}{\partial \mathbf{u}_h} & -\frac{\partial \mathbf{R}_1}{\partial d_h} \end{bmatrix} \begin{bmatrix} \Delta \mathbf{u}_h \\ \Delta d_h \end{bmatrix} = \begin{bmatrix} \mathbf{R}_0 \\ \mathbf{R}_1 \end{bmatrix} \quad (25)$$

where,  $\Delta \mathbf{u}_h = \mathbf{u}_h^k - \mathbf{u}_h^{k-1}$ ,  $\Delta d_h = d_h^k - d_h^{k-1}$ , and  $\mathbf{u}_h^k, d_h^k$  are the solutions at the  $k$ -th iteration. Thus, the element stiffness matrix can be:

$$\begin{aligned}
 -\frac{\partial \mathbf{R}_0}{\partial \mathbf{u}_h} &= \frac{\partial}{\partial \mathbf{u}_h} (\boldsymbol{\sigma}(\mathbf{u}_h), \boldsymbol{\varepsilon}(\boldsymbol{\Phi}))_\Omega \\
 -\frac{\partial \mathbf{R}_0}{\partial d_h} &= \frac{\partial \boldsymbol{\sigma}}{\partial d_h} (\nabla \boldsymbol{\Phi}^T, \phi)_\Omega \\
 -\frac{\partial \mathbf{R}_1}{\partial \mathbf{u}_h} &= -2(1 - d_h) \frac{\partial \mathcal{H}}{\partial \boldsymbol{\varepsilon}} (\phi^T, \nabla \boldsymbol{\Phi})_\Omega \\
 -\frac{\partial \mathbf{R}_1}{\partial d_h} &= 2(\phi^T \mathcal{H}, \phi)_\Omega + G_c l_0 (\nabla \phi^T, \nabla \phi)_\Omega + \frac{G_c}{l_0} (\phi^T, \phi)_\Omega,
 \end{aligned} \tag{26}$$

where the derivative of the stress tensor with respect to the displacement:

$$\frac{\partial}{\partial \mathbf{u}_h} (\boldsymbol{\sigma}(\mathbf{u}_h), \boldsymbol{\varepsilon}(\boldsymbol{\Phi}))_\Omega = \frac{\partial \boldsymbol{\sigma}}{\partial \boldsymbol{\varepsilon}} (\boldsymbol{\varepsilon}(\boldsymbol{\Phi}), \boldsymbol{\varepsilon}(\boldsymbol{\Phi}))_\Omega.$$

Because the total energy is a non convex function of the overall unknown quantity  $(\mathbf{u}, d)$ , but it is a separate convex function of displacement  $\mathbf{u}$  or phase field  $d$ . Therefore, in a robust Staggered strategy,  $\frac{\partial \mathbf{R}_1}{\partial \mathbf{u}_h}, \frac{\partial \mathbf{R}_0}{\partial d_h}$  can be ignored, to independently solve for the displacement variable  $\mathbf{u}_h$  and the phase field variable  $d_h$ . This independence simplifies the problem and allows for separate updates of these variables without direct coupling in every iteration or time step. In this article, we use the linear element method, so we can use the method of no numerical integration for matrix assembly, including  $(\phi, \phi)_\Omega$ . Here, we will not elaborate further. The specific content can be found in the FEALPy software package[37].

### 3.2 An adaptive method based on recovery type posterior error estimates

In this paper, we use a recovery-type posterior error estimates method for error calculation, which is based on post-processing techniques. The commonly used methods are: weighted average, least squares, local or global projection, etc. The post-processed solution is used instead of the gradient of the true solution and the numerical solution for error estimates[44, 43]. Based on the characteristics of the phase field function, it can be inferred that the distribution of the phase field can effectively capture the occurrence of cracks. Therefore, we use the phase field function for posterior error estimates.

The process of the adaptive mesh refinement algorithm based on posterior error estimates is as follows: after the numerical solution is calculated on the current mesh, the element error and global error are estimated by using the posterior error estimates. The cells that need to be refined are labeled according to the calculated element error and the selected labeling strategy, and finally, the selected refinement method is used to refine the mesh.

Below is an introduction to commonly used gradient recovery methods. The simple averaging method is:

$$\mathcal{R}_h d_h(\mathbf{x}) = \frac{1}{m_{\mathbf{x}}} \sum_{\tau \in \Gamma_{\mathbf{x}}} \nabla d_h(\mathbf{x})|_{\tau}.$$

Here,  $m_{\mathbf{x}}$  is the number of elements with node  $\mathbf{x}$  as the vertex, and  $\Gamma_{\mathbf{x}}$  is the set of elements with node  $\mathbf{x}$  as the vertex.

Area averaging method is:

$$\mathcal{R}_h d_h(\mathbf{x}) = \frac{\sum_{\tau \in \Gamma_{\mathbf{x}}} |\tau| \nabla d_h(\mathbf{x})|_{\tau}}{\sum_{\tau \in \Gamma_{\mathbf{x}}} |\tau|}.$$

Here,  $|\tau|$  represents the area of element  $\tau$ .

Harmonic area averaging method is:

$$\mathcal{R}_h d_h(\mathbf{x}) = \frac{\sum_{\tau \in \Gamma_{\mathbf{x}}} \frac{1}{|\tau|} \nabla d_h(\mathbf{x})|_{\tau}}{\sum_{\tau \in \Gamma_{\mathbf{x}}} \frac{1}{|\tau|}}.$$

Angle averaging method is:

$$\mathcal{R}_h d_h(\mathbf{x}) = \frac{\sum_{\tau \in \Gamma_{\mathbf{x}}} \alpha_{\tau} \nabla d_h(\mathbf{x})|_{\tau}}{\sum_{\tau \in \Gamma_{\mathbf{x}}} \alpha_{\tau}}.$$

Here,  $\alpha_{\tau}$  represents the degree of the angle of element  $\tau$  with a vertex of  $\mathbf{x}$ .

Distance average is:

$$\mathcal{R}_h d_h(\mathbf{x}) = \frac{\sum_{\tau \in \Gamma_{\mathbf{x}}} l_{\tau} \nabla d_h(\mathbf{x})|_{\tau}}{\sum_{\tau \in \Gamma_{\mathbf{x}}} l_{\tau}}.$$

Here,  $l_{\tau}$  represents the distance from the center of gravity of element  $\tau$  to  $\mathbf{x}$ .

On the element  $\tau$ , let  $\mathcal{R}_h$  be the gradient reconstruction operator, and for the phase field  $d$  there is:

$$\eta_{\tau} = \|\mathcal{R}_h d_h - \nabla d_h\|_{0,\tau}.$$

The above equation can be used to estimate the error  $\|\nabla e_h\|_{0,\tau}$ . If  $\mathcal{R}_h$  is super-convergent [45], then

$$\|\mathcal{R}_h d_h - \nabla d_h\|_{0,\Omega} = o(\|\nabla d - \nabla d_h\|_{0,\Omega}),$$

therefore,

$$\frac{\|\mathcal{R}_h d_h - \nabla d_h\|_{0,\Omega}}{\|\nabla d - \nabla d_h\|_{0,\Omega}} = \frac{\|(\mathcal{R}_h d_h - \nabla d) + (\nabla d - \nabla d_h)\|_{0,\Omega}}{\|\nabla d - \nabla d_h\|_{0,\Omega}} \rightarrow 1.$$

The posterior error estimate obtained in this case is asymptotically accurate. Based on the calculated posterior error estimates, the error on each element can be obtained. Units with larger errors are selected for refinement, and the error size is judged according to the labeling strategy to determine whether it meets the standard. Detailed theories and application examples can be found in papers such as [51, 52, 53, 54]. There are two commonly used labeling strategies, where  $\eta$  is the total estimates error,  $\eta_{\tau}$  is the estimates error on element  $\tau$ , and  $0 < \theta < 1$  is the labeling parameter.

- The Maximum Criterion method: Make  $\eta_{\max} = \max_{\tau \in \Gamma} \eta_{\tau}$ , mark the elements of  $\eta_{\tau} > \theta \eta_{\max}$ .
- The  $L^2$  Criterion method: Sort the element estimates errors and place the corresponding elements in the labeled element set  $\mathcal{M}$  from largest to smallest, until  $\sum_{\tau \in \mathcal{M}} \eta_{\tau}^2 > \theta \eta^2$  is satisfied.

### 3.3 Overall Algorithm Process

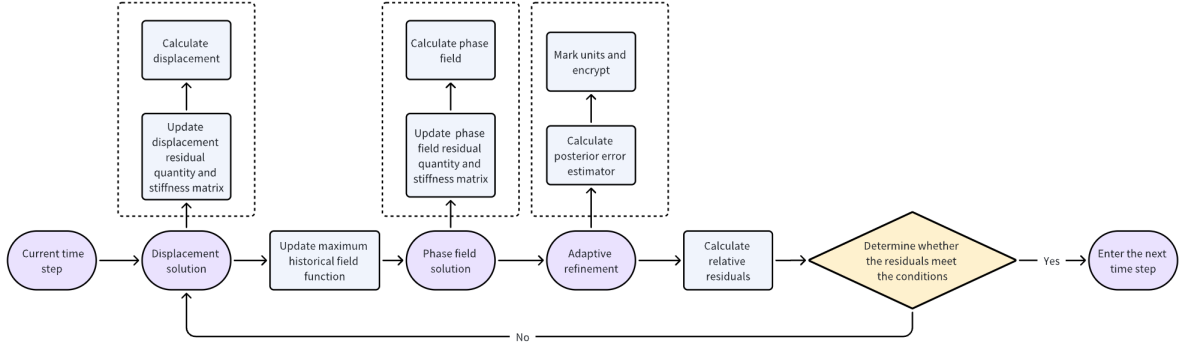


Figure 1: Algorithm Flow

Based on FEALPy[37], we have developed the program in a modular fashion, employing a unified interface to significantly enhance the flexibility and efficiency of experimental testing. Figure 1 is the overall algorithm implementation flowchart. Each algorithm's program module is independent, allowing for the selection of appropriate calculation methods. In our program design, the choice of solution method is dimension-agnostic, allowing independent selection of adaptive mesh refinement for both 2D and 3D calculations.

To optimize the algorithm, we have introduced a matrix calculation method without numerical integration assembly in the matrix assembly module. Additionally, in solving algebraic equation systems, we have integrated various methods including direct solvers, iterative solvers [57], and GPU iterative solvers [55]. It allows for the selection of appropriate methods, resulting in significant computational efficiency gains. For Mesh refinement methods, bisect refinement and triangle red-green refinement based on half-edge-mesh can be selected according to the characteristics of the mesh.

The simulations are performed on a machine with the following specifications:

- **Memory:** 64.0 GiB

**Algorithm 1** Solve Process

 1: **for** the iterations  $k$  and the current time step  $n$  **do**

 2: calculate the displacement stiffness matrix  $-\left(\frac{\partial \mathbf{R}_0}{\partial \mathbf{u}_h}\right)^k$  and the right-hand side term  $\mathbf{R}_0^k$ .

 3: solve for displacement  $\mathbf{u}_h^{k+1}$ :

$$-\left(\frac{\partial \mathbf{R}_0}{\partial \mathbf{u}_h}\right)^k \Delta \mathbf{u}_h^k = \mathbf{R}_0^k, \quad \mathbf{u}_h^{k+1} = \mathbf{u}_h^k + \Delta \mathbf{u}_h^k,$$

 4: substitute  $\mathbf{u}_h^{k+1}$  into the  $\mathcal{H}$  function to obtain:

$$\mathcal{H}^{k+1}(\mathbf{u}_h^{k+1}) = \max e^+(\varepsilon(\mathbf{u}_h^{k+1})),$$

 5: using the updated  $\mathcal{H}$  function, calculate the phase field stiffness matrix  $-\left(\frac{\partial \mathbf{R}_1}{\partial d_h}\right)^k$  and the right-hand side term  $\mathbf{R}_1^k$ .

 6: solve for the phase field value  $d_h^{k+1}$ :

$$-\left(\frac{\partial \mathbf{R}_1}{\partial d_h}\right)^k \Delta d_h^k = \mathbf{R}_1^k, \quad d_h^{k+1} = d_h^k + \Delta d_h^k.$$

 7: calculate the posterior error estimate  $\eta$ , adaptive mesh refinement.

 8: compute the relative residual  $error = \max \left\{ \frac{\|\mathbf{R}_0^{(n+1)}\|}{\|\mathbf{R}_0^{(0)}\|}, \frac{\|\mathbf{R}_1^{(n+1)}\|}{\|\mathbf{R}_1^{(0)}\|} \right\}$ .

 9: **if** error  $< 1e - 5$  **then**

 10:  $k + 1$ .

 11: **else**

 12:  $n + 1$ .

 13: **end if**

 14: **end for**

- **Processor:** Intel® Xeon(R) Gold 5118 CPU @ 2.30GHz  $\times$  48 cores
- **Graphics:** NVIDIA Corporation GP107GL [Quadro P620]

Table 1: Comparison of Solve Times with and without GPU for a 3D Model

	GPU (Iterative)	CPU (Iterative)	CPU (Direct)
Displacement Solve Time (seconds)	4.90454	14.18117	12391.396
Phase Field Solve Time (seconds)	0.01722	0.07701	64.9935

The table (1) compares the computational performance for solving a 3D model with 56,729 nodes, using GPU acceleration versus CPU processing. It presents the solve times for both displacement and phase field calculations under different methods.

Displacement solve time: Using GPU, the time required to solve displacement is 4.90454 seconds. In comparison, using the CPU with the iterative method takes 14.18117 seconds, and the direct method takes 12391.396 seconds. The GPU solution is approximately 65.5% faster than the iterative method and about 99.96% faster than the direct method.

Phase field solve time: For phase field calculations, the GPU solution takes 0.01722 seconds. The CPU iterative method requires 0.07701 seconds, while the direct method takes 64.9935 seconds. The GPU solution is approximately 77.6% faster than the iterative method and about 99.97% faster than the direct method.

Overall, the use of GPU acceleration results in substantial time savings and improved computational efficiency, making these techniques highly advantageous in practical applications, especially for solving large-scale 3D models.



## 4 Algorithm validation and application

We test several classical examples, namely: a model with a rigid circular inclusion embedded in a square plate, a model with a unilateral notch in which the plate is subjected to tensile and shear forces, an L-shaped plate with mixed tensile and compressive loads, and a 3D model with a single slice under tensile force.

### 4.1 Square Model with a Circular Notch: Upward Stretch on the Upper Boundary

A rigid circular inclusion is embedded in a square plate, and a vertical displacement is applied to its top surface. The computational domain  $\Omega$  is a rectangular region  $[0, 1] \times [0, 1]$  with a circular cutout centered at  $(0.5, 0.5)$ , having a radius of 0.2, Figure 2 shows the geometric shape of the model. For the phase field on the boundaries, zero Dirichlet boundary conditions are applied. Parameters are given as follows:  $G_c = 1$ ,  $l_0 = 0.02$ ,  $E = 200$ ,  $\nu = 0.2$ [14].

Boundary conditions are as follows:

- Dirichlet boundary at the upper boundary  $y = 1$ , with displacement increments as follows for the first 5 steps:  $\Delta u_y = 1.4 \times 10^{-2}$  mm, and for the subsequent 25 steps:  $\Delta u_y = 2.2 \times 10^{-3}$  mm;
- Internal boundary: Displacement is 0 along the boundary of the circular hole.

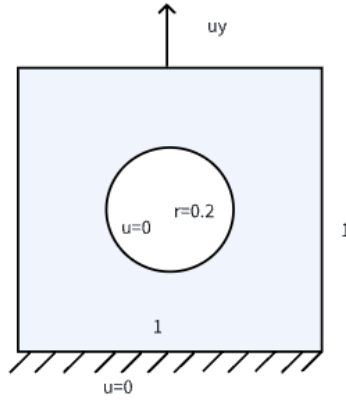


Figure 2: Geometry and boundary conditions of the square model with a circular notch (the unit is mm)

As shown in Figure 3, the adaptive finite element simulation displays the final phase field values, crack states, and the resulting mesh refinement. With an initial mesh size of 0.05, the mesh is automatically refined in regions that require higher accuracy during the simulation. This dynamic refinement results in an increase in the number of mesh elements from 640 to 9558, ensuring high simulation accuracy. The adaptive refinement approach significantly improves computational efficiency, completing the entire simulation in only 86 seconds.

In contrast, if the adaptive refinement is not used, we must ensure that the mesh size  $h < l_0/2$ . At this point, the non-adaptive simulation utilizes a fine mesh size of 0.01 from the start and maintains a constant mesh element of 19224 throughout the simulation. While this guarantees uniform high accuracy throughout the simulation domain, it also results in wasted computational resources in regions where finer meshes are not necessary. Consequently, the simulation time is significantly longer, taking 695 seconds to complete.

Despite the differences in mesh refinement and simulation time, the results from both the adaptive and non-adaptive simulations exhibit a high degree of consistency in terms of the computed phase field values and crack states. However, the adaptive refinement method stands out as a preferred approach due to its ability to balance computational accuracy and efficiency through dynamic mesh refinement.

Figure 4 demonstrates the evolution of residual force throughout the fracture process under an external load. During the initial loading of displacement, the residual force gradually increases. Upon the occurrence of fracture, the stored potential energy begins to convert into fracture energy, resulting in a gradual decrease in the residual force until the material completely breaks, at which point the residual force becomes zero. The trends in the simulations, both with and without adaptive mesh refinement, remain consistent. This result is consistent with the result obtained by Bourdin[14].

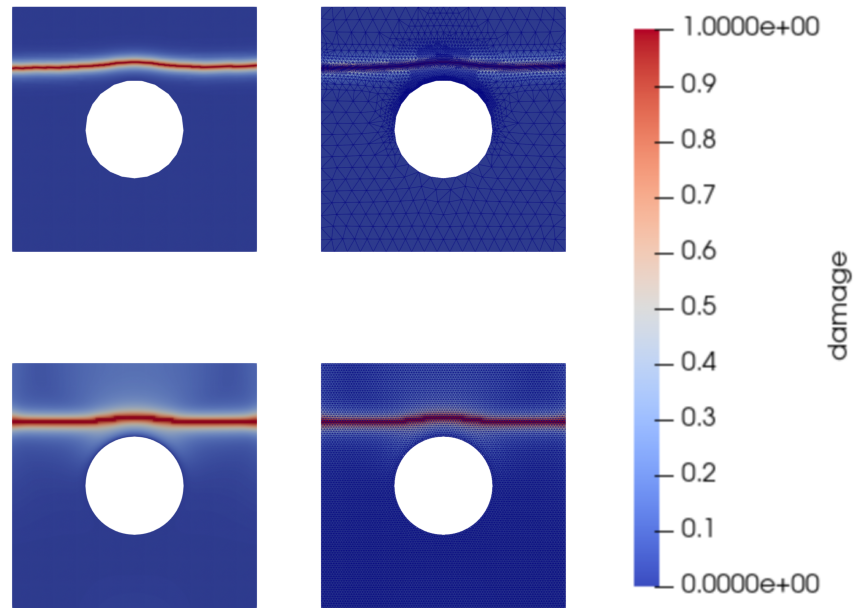


Figure 3: The final results of the square model with a circular notch. The upper figures show the results of adaptive mesh refinement (initial mesh size  $h=0.05$ ), and the lower figures show the results without using adaptive (mesh size  $h=0.01$ ). The left figures show the final phase field values, and the right figures show the final mesh situation.

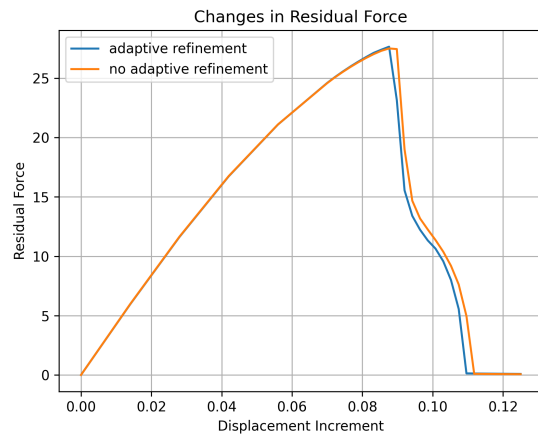


Figure 4: Residual force with load-displacement curves of the square model with a circular notch, adaptive and non-adaptive

The adaptive mesh refinement approach enables a more targeted refinement of the mesh in regions of interest, such as around crack tips, resulting in improved accuracy in capturing the energy evolution. In summary, Figure 4 highlights the role of adaptive mesh refinement in improving the accuracy of simulations while maintaining consistency in the observed residual force changes during fracture.

#### 4.2 Model with a Notch: Upward Stretch on the Upper Boundary in the $y$ Direction

Consider a square model with a unilateral incision, as shown in Figure 5. The model has the following material parameters: the critical energy release rate is given by  $G_c = 2.7 \times 10^{-3}$  kN/mm, the scale factor  $l_0 = 1.33 \times 10^{-2}$  mm, Lamé's first parameter  $\lambda = 121.15$  kN/mm<sup>-2</sup>, and Lamé's second parameter  $\mu = 80.77$  kN/mm<sup>-2</sup>[31].

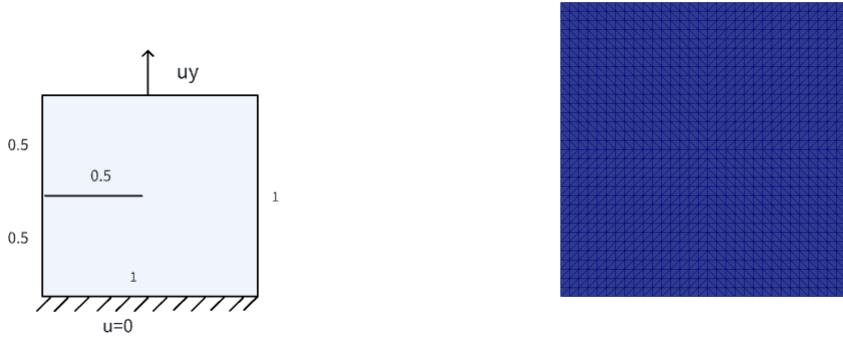


Figure 5: Geometry and boundary conditions of the model with a notch (the unit is mm) and initial mesh generation of the model with a notch

The material's bottom boundary at  $y = 0$  is fixed in place. The upper boundary at  $y = 1$  experiences a displacement increment of  $\Delta u_y = 1 \times 10^{-5}$  mm for the initial 500 steps, followed by an increment of  $\Delta u_y = 1 \times 10^{-6}$  mm for subsequent steps, with a total displacement of  $u_y = 6.1 \times 10^{-3}$  mm.

Figure 6 illustrates the adaptive refinement of the mesh during the crack growth process at three distinct stages. Initially, the model starts with a coarse mesh consisting of 2048 elements. As the load is incrementally applied, the mesh undergoes adaptive refinement to accurately capture the evolving crack geometry. If we do not use adaptive refinement, the number of elements should not be less than 45000 to ensure the accuracy of the simulation. So the adaptive refinement method significantly reduces the number of elements and improves the computational efficiency.

At the first stage, with an incremental displacement of  $\Delta u_y = 0.0055$  mm applied, the mesh elements increase to 3406. This refinement is concentrated around the crack tip and along the expected crack path, indicating that the simulation is anticipating the direction of crack propagation.

At the second stage, with an additional displacement of  $\Delta u_y = 0.0059$  mm, the mesh elements further increase to 6040. The refinement continues to focus on the crack tip and the surrounding region, ensuring that the simulation captures the fine details of the crack growth.

Finally, with a further displacement of  $\Delta u_y = 0.006$  mm, the mesh elements expand to 7510. The adaptive refinement continues to evolve, maintaining a high resolution in the critical regions while minimizing the number of elements in less important areas.

Figure 7 depicts the evolution of residual force at the node where the load is applied during the loading process. Notably, the observed outcome closely aligns with the previous findings reported by Miehe[10, 11] and Ambati et al. using conventional phase field model (PFM) calculations. This consistency strengthens the credibility of the current results and highlights the reliability of the adaptive finite element simulation approach.

#### 4.3 Model with a Notch: Shearing Stretch on the Upper Boundary in the $x$ -Direction

The model parameters are consistent with those used in the previous model, with the main change being the modification of the direction of displacement increment. Specifically, while retaining all other boundary conditions and model parameters, replace the shear force on the right side with the upward tension in the above model to verify the accuracy of simulating type II fracture[31].

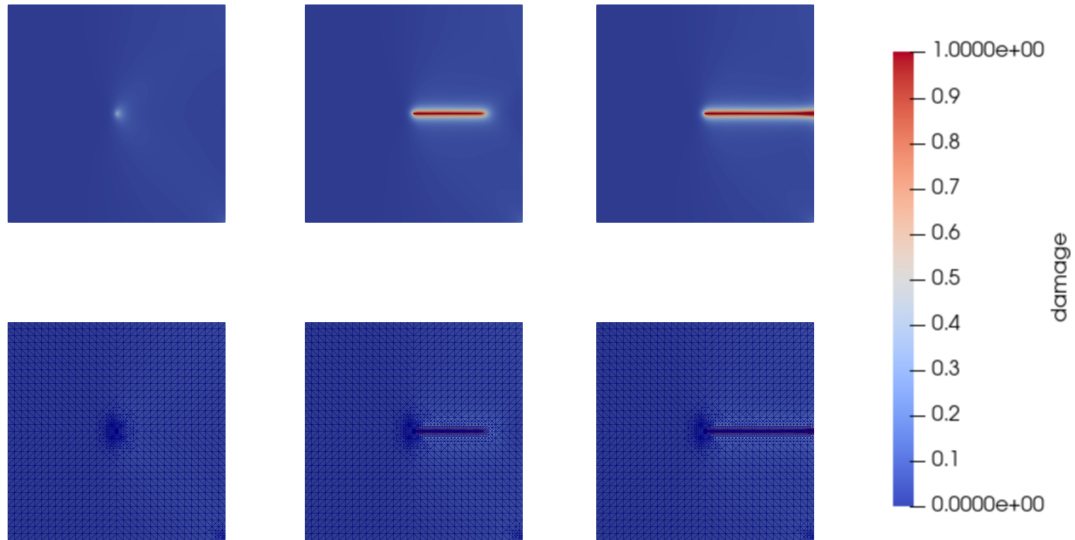


Figure 6: The phase field value (upper) and the mesh refinement situation (lower) of the model with a notch (stretch), under different displacement loading conditions, from left to right  $\Delta u_y$  in order 0.0055 mm, 0.0059 mm, 0.006 mm

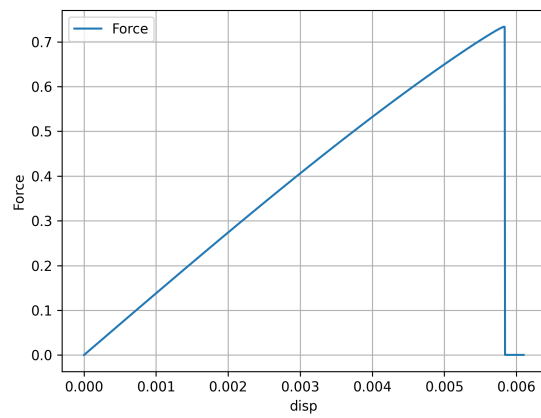


Figure 7: Load-displacement curves in the model with a notch (stretch)

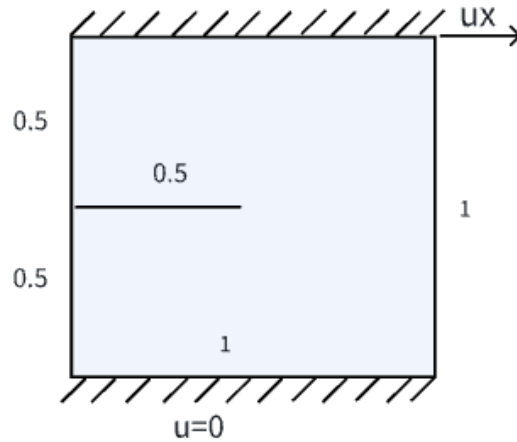


Figure 8: Geometry and boundary conditions of the model with a notch (the unit is mm)

At each step of the upper boundary where  $y = 1$ , the displacement increment is  $\Delta u_x = 1 \times 10^{-5}$  mm, and it loads 1700 steps. The total displacement increment is  $u_x = 1.7 \times 10^{-2}$  mm. The bottom of the material is fixed at  $y = 0$ . Figure 8 shows the geometric shape of the model and the initial mesh generation.

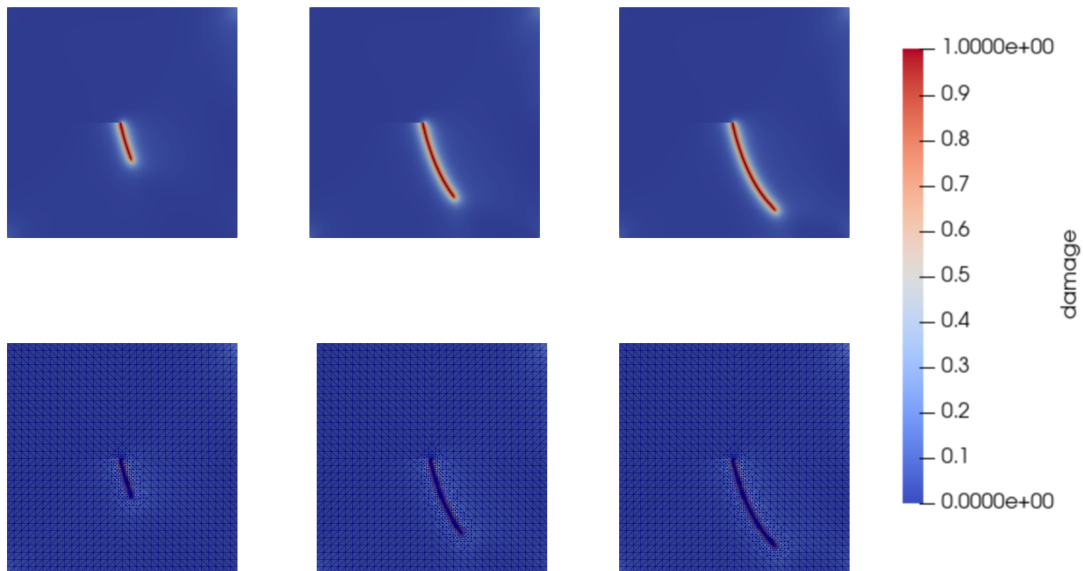


Figure 9: The phase field value (upper) and the mesh refinement situation (lower) of the model with a notch (shearing), under different displacement loading conditions, from left to right  $\Delta u_x$  in order 0.012 mm, 0.015 mm, 0.017 mm, 0.021 mm

Figure 9 shows the mesh refinement patterns and phase field values for varying displacement loadings in the  $x$ -direction. As the load increases ( $\Delta u_x = 0.012$  mm, 0.015 mm, 0.017 mm, 0.021 mm), cracks gradually form, and the mesh

elements transition from 2048 to 3786, 5540, 6226, and 7098. Notably, the mesh refinement consistently aligns with and outpaces crack generation, enabling early capture of the crack propagation direction.

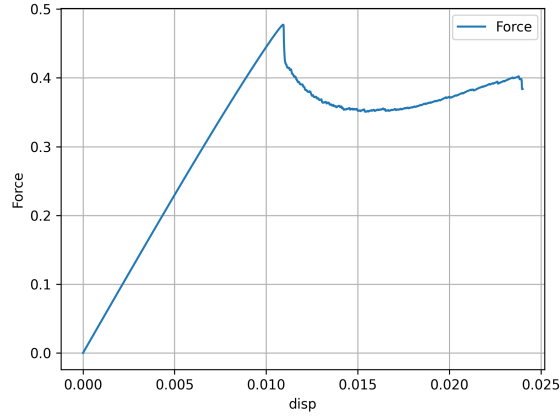


Figure 10: Load-displacement curves in the model with a notch (shearing)

Figure 10 illustrates the load-displacement curves for the unilateral incision model. The variation of residual force in the stressed region upon load application exhibits consistency with results obtained by Miehe and Ambati using standard phase field model calculations.

These computational results demonstrate that the algorithm effectively simulates both type I and type II fractures through adaptive mesh refinement, enhancing computational efficiency without compromising accuracy. The alignment of mesh refinement with crack propagation further validates the algorithm's ability to accurately capture fracture behavior.

#### 4.4 The L-shaped plate (Stretch and compression mixing)

Consider an L-shaped region, the model has the following material parameters. The critical energy release rate is given by  $G_c = 8.9e - 5$  kN/mm, the scale factor  $l_0 = 1.88$  mm, the Lamé's first parameter  $\lambda = 6.16$  kN/mm<sup>-2</sup>, and the Lamé's second parameter  $\mu = 10.95$  kN/mm<sup>-2</sup>. Figure 11 shows the geometric shape of the model and the initial mesh generation[31].

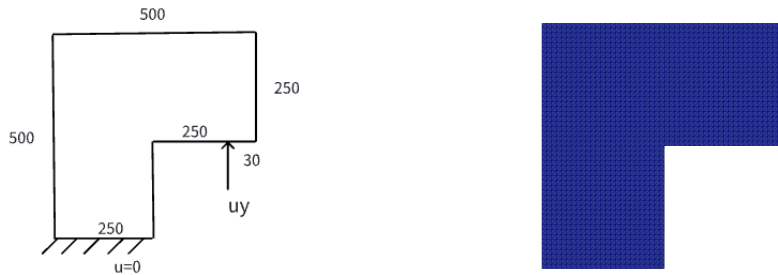


Figure 11: Geometry and boundary conditions of the L-shaped plate (the unit is mm) (left), and initial mesh generation of the model (right)

For this model, we impose a tension-compression mixed load condition at a point, with specific parameters as illustrated in Figure12. Initially, an upward load is applied, followed by a downward load, and then an upward load again. The purpose of this loading sequence is to assess the algorithm's capability to handle compression crack closure under tension-compression mixed conditions.

In Figure 13, we observe significant changes in the mesh refinement patterns and corresponding phase field values as displacement loading conditions vary. These changes are presented sequentially from left to right, corresponding to

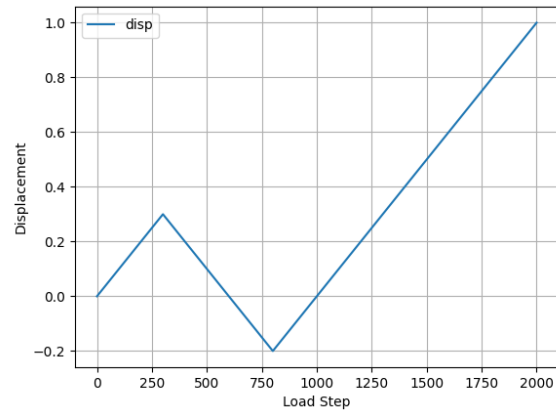


Figure 12: Displacement loading situation of the L-shaped plate

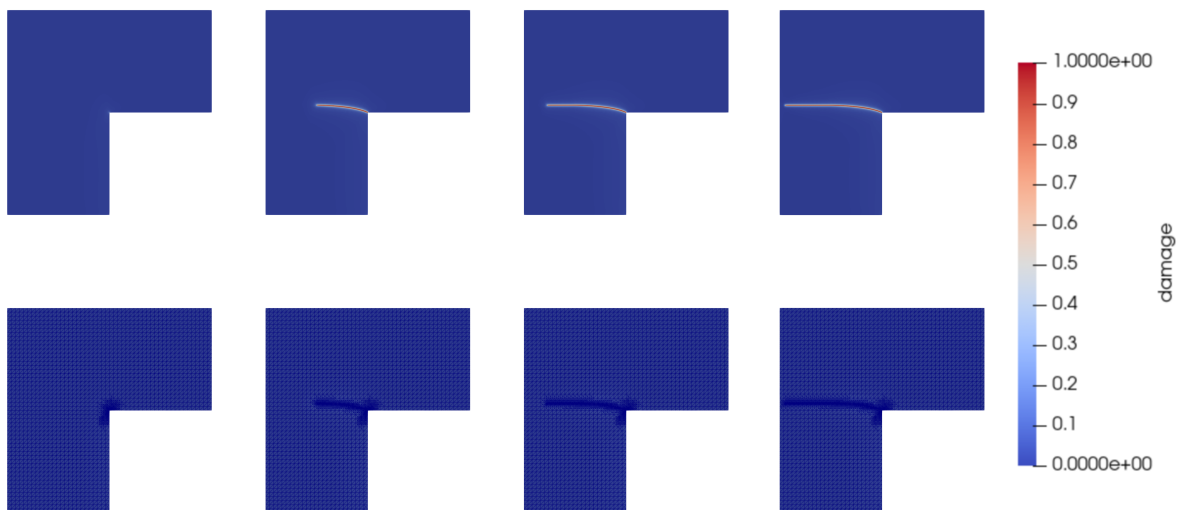


Figure 13: The phase field value (upper) and the mesh refinement situation (lower) of the L-shaped plate, under different displacement loading conditions, from left to right  $\Delta u_y$  in order 0.22 mm, 0.3 mm, 0.45 mm, 1 mm

different displacement values of  $\Delta u_y = 0.22 \text{ mm}, 0.3 \text{ mm}, 0.45 \text{ mm}, 1 \text{ mm}$ . As the load is gradually applied, cracks form progressively in the simulated L-shaped plate.

It is worth noting that the number of mesh elements also changes during the process of crack formation and propagation. Starting with an initial count of 3750 mesh elements, the number increases to 6563, 22549, 31265, and ultimately reaches 34419 as cracks emerge and propagate. Under compression conditions, once a crack forms, it does not close, reflecting the irreversibility of crack propagation. This characteristic is crucial for understanding and predicting the failure behavior of materials under compressive loads.

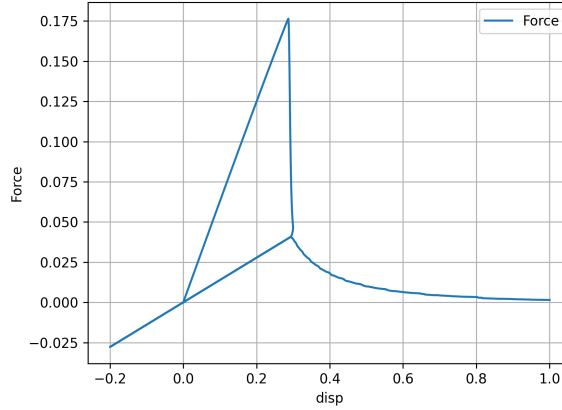


Figure 14: Load-displacement curves of the L-shaped plate

Additionally, Figure 14 illustrates the variation of residual force with the application of load, showing excellent agreement with results calculated by Singh et al.

#### 4.5 3D model with planar cutouts: Upward Stretch on the Upper Boundary in the $z$ Direction

For a 3D model featuring planar slices, the model parameters are set as follows: a critical energy release rate of  $G_c = 5e - 4 \text{ kN/mm}$ , a scale factor of  $l_0 = 0.2 \text{ mm}$ , Young's modulus  $E = 20.8 \text{ KN/mm}^2$ , and Poisson's ratio  $\nu = 0.3$ [22].

The boundary conditions in this model resemble those of a 2D extruded model. An upward displacement is applied at the upper boundary located at  $z = 10$ , with an increment of  $\Delta u_z = 1 \times 10^{-4} \text{ mm}$  resulting in a total displacement increment of  $u_z = 4.5 \times 10^{-2} \text{ mm}$ . The bottom of the material is fixed at  $z = 0$ . Figure 15 shows the geometric shape of the model and the initial mesh generation.

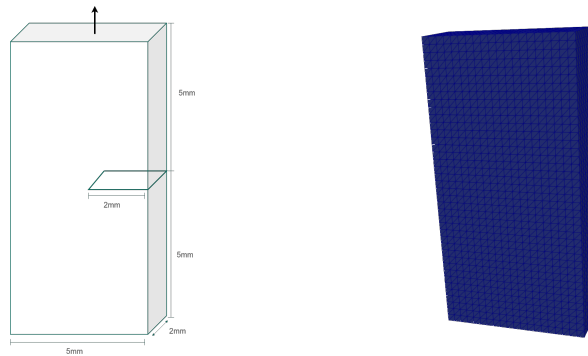


Figure 15: Geometry and boundary conditions (the unit is mm) (left), and initial mesh generation of the 3D model (right)

In the three-dimensional example, we employed a tetrahedral mesh for initial mesh generation, utilizing the bisection method for mesh refinement during the adaptive process.



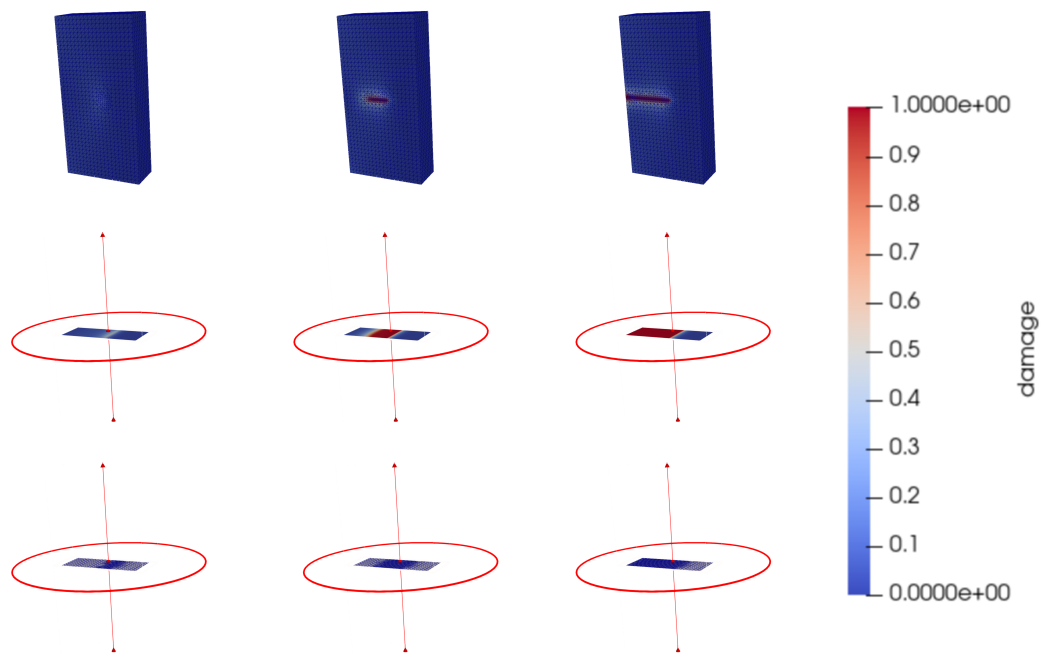


Figure 16: The phase field value (upper) and the mesh refinement situation (lower) of the 3D model, under different displacement loading conditions, from left to right  $\Delta u_z$  in order 0.27 mm, 0.28 mm, 0.29 mm

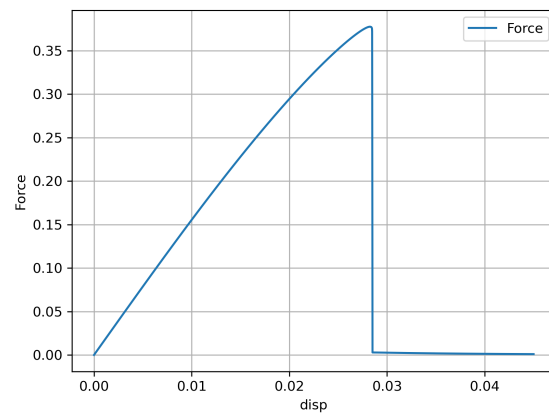


Figure 17: Load-displacement curves of the 3D model

By examining the variation diagram of residual force, we can observe that the results obtained from the three-dimensional simulation are in good agreement with those of the corresponding two-dimensional calculations. This consistency validates the applicability and reliability of the chosen numerical methods in both two- and three-dimensional settings. Furthermore, the trend of mesh refinement observed in the three-dimensional simulation aligns closely with the direction of crack development. As the load is gradually applied, cracks begin to form, and the number of mesh elements increases accordingly from the initial 38400 to 52352, 64328, and ultimately 82289. This progressive refinement ensures that the mesh maintains adequate resolution in areas where crack propagation is occurring, thereby improving the accuracy of the simulation results.

## 5 Summary

This paper presents an adaptive finite element method (AFEM) for phase field fracture models, leveraging recovery-type posterior error estimates to achieve efficient mesh refinement. The method transforms the gradient of the numerical phase field into a smoother function space, using the discrepancy between the recovered and original gradients as an error indicator. This approach eliminates the need for empirical parameters, allowing the automatic and accurate capture of crack propagation directions while significantly reducing the number of mesh elements and improving computational efficiency. By integrating these innovations into the FEALPy platform, we have implemented a robust phase field fracture simulation module with flexible refinement techniques and GPU-accelerated matrix solvers. Numerical experiments on classical 2D and 3D brittle fracture problems validate the accuracy, robustness, and efficiency of the proposed method.

In future work, we plan to expand this framework by developing a dedicated fracture numerical simulation application (APP) built on FEALPy. This APP will serve as a comprehensive platform for the integration, validation, and comparison of various fracture simulation algorithms, providing a rich library of computational examples. Leveraging FEALPy's modular architecture, multi-backend tensor computation engine, and extensive algorithmic support, the APP will offer diverse simulation capabilities, supporting scalable tensor computation with backend options such as Numpy, PyTorch, and JAX. The application will harness FEALPy's powerful functionality, including hierarchical and modular structures, and an array of core algorithms, to facilitate seamless, high-performance simulations on heterogeneous hardware systems. Additionally, the APP will enable the generation of large-scale datasets for machine learning models, fostering interdisciplinary research in fracture mechanics and intelligent simulation technologies.

## Acknowledgments

This work were supported by the National Natural Science Foundation of China (NSFC) (Grant Nos. 12371410, 12261131501), the construction of innovative provinces in Hunan Province (Grant No. 2021GK1010), and the Graduate Innovation Project of Xiangtan University (Nos. XDCX2023Y135, XDCX2024Y175).

During the preparation of this work the author(s) used ChatGPT 4o in order to improve language and readability. After using this tool/service, the author(s) reviewed and edited the content as needed and take(s) full responsibility for the content of the publication.

## References

- [1] Anderson, T. L. *Fracture Mechanics: Fundamentals and Applications* (4th ed.). CRC Press, 2017.
- [2] Lemaitre, J., Desmorat, R. *Engineering Damage Mechanics: Ductile, Creep, Fatigue and Brittle Failures*. Springer, 2005.
- [3] Bazant, Z. P., Planas, J. *Fracture and Size Effect in Concrete and Other Quasibrittle Materials*. CRC Press, 1998.
- [4] Broek, D. *Elementary Engineering Fracture Mechanics*. Springer Science & Business Media, 2012.
- [5] Newman, J. C. A crack opening stress equation for fatigue crack growth. *International Journal of Fracture*, 2008, 151(3), 207-214.
- [6] Barenblatt, G. I. The mathematical theory of equilibrium cracks in brittle fracture. *Advances in Applied Mechanics*, 1959, 7, 55-129.
- [7] Griffith, A. A. The phenomena of rupture and flow in solids. *Philosophical Transactions of the Royal Society of London A*, 1921, 221, 163-198.
- [8] Irwin, G. R. Fracture dynamics. In: *Fracturing of Metals*, American Society for Metals, Cleveland, Ohio, pp. 147-166, 1948.

- [9] Irwin, G. R. Analysis of stresses and strains near the end of a crack traversing a plate. *Journal of Applied Mechanics*, 1957, 24, 361-364.
- [10] Miehe, C., Hofacker, M., Welschinger, F. A phase field model for rate-independent crack propagation: Robust algorithmic implementation based on operator splits. *Computer Methods in Applied Mechanics and Engineering*, 2010, 199, 2765-2778.
- [11] Miehe, C., Welschinger, F., Hofacker, M. Thermodynamically consistent phase-field models of fracture: Variational principles and multi-field FE implementations. *International Journal for Numerical Methods in Engineering*, 2010, 83, 1273-1311.
- [12] Amor, H., Marigo, J.-J., Maurini, C. Regularized formulation of the variational brittle fracture with unilateral contact: Numerical experiments. *Journal of the Mechanics and Physics of Solids*, 2009, 57, 1209-1229.
- [13] Ambati, M., Gerasimov, T., De Lorenzis, L. A review on phase-field models of brittle fracture and a new fast hybrid formulation. *Computational Mechanics*, 2015, 55, 383-405.
- [14] Bourdin, B., Francfort, G. A., Marigo, J. J. Numerical experiments in revisited brittle fracture. *Journal of the Mechanics and Physics of Solids*, 2000, 48(4), 797-826.
- [15] Shen, Y., Mollaali, M., Li, Y., et al. Implementation Details for the Phase Field Approaches to Fracture. *Journal of Shanghai Jiaotong University (Science)*, 2018, 23(01), 166-174.
- [16] Muñoz-Reja, M., Buroni, F., Sáez, A., et al. 3D explicit-BEM fracture analysis for materials with anisotropic multifield coupling. *Applied Mathematical Modelling*, 2016, 40(4), 2897-2912.
- [17] Babuska, I., Rheinboldt, W. Error estimates for adaptive finite element computations. *SIAM J. Numerical Analysis*, 1978, 15, 736-754.
- [18] Babuska, I., Rheinboldt, W. Reliable Error Estimation and Mesh Adaptation for the Finite Element Method. In: *Computational Methods in Nonlinear Mechanics*, North-Holland Publishing Co., 1980, pp. 67-107.
- [19] Babuska, I., Miller, A. A Posteriori Error Estimates and Adaptive Techniques for the Finite Element Method. University of Maryland, Technical Note BN-968, 1981.
- [20] Ruvin, D. W., Sundararajan, N., Greg, Y., et al. Adaptive phase-field modelling of fracture propagation in poroelastic media using the scaled boundary finite element method. *Computer Methods in Applied Mechanics and Engineering*, 2023, 411.
- [21] Wu, J. Y., Nguyen, V. P. A length scale insensitive phase-field damage model for brittle fracture. *Journal of the Mechanics and Physics of Solids*, 2018, 119, 20-42.
- [22] Li, S., Tian, L., Cui, X. Phase field crack model with diffuse description for fracture problem and implementation in engineering applications. *Advances in Engineering Software*, 2019, 129, 44-56.
- [23] Borden, M. J. Isogeometric analysis of phase-field models for dynamic brittle and ductile fracture. PhD thesis, University of Texas at Austin, 2012.
- [24] Karma, A., Kessler, D. A., Levine, H. Phase-field model of mode III dynamic fracture. *Physical Review Letters*, 2001, 87(4), 045501.
- [25] Sargado, J. M., Keilegavlen, E., Berre, I., Nordbotten, J. M. High-accuracy phase-field models for brittle fracture based on a new family of degradation functions. *Journal of the Mechanics and Physics of Solids*, 2017, doi:10.1016/j.jmps.2017.10.015.
- [26] Assaf, R., Birk, C., Natarajan, S., Gravenkamp, H. Three-dimensional phase-field modeling of brittle fracture using an adaptive octree-based scaled boundary finite element approach. *Computer Methods in Applied Mechanics and Engineering*, 2022, 399.
- [27] Benson, D. J., Bazilevs, Y., de Luycker, E., Hsu, M. C., Scott, M., Hughes, T. J. R., Belytschko, T. A generalized finite element formulation for arbitrary basis functions: From isogeometric analysis to XFEM. *International Journal for Numerical Methods in Engineering*, 2010, 83, 765-785.
- [28] De Luycker, E., Benson, D. J., Belytschko, T., Bazilevs, Y., Hsu, M. C. X-FEM in isogeometric analysis for linear fracture mechanics. *International Journal for Numerical Methods in Engineering*, 2011, 87, 541-565.
- [29] Ghorashi, S. S., Valizadeh, N., Mohammadi, S. Extended isogeometric analysis for simulation of stationary and propagating cracks. *International Journal for Numerical Methods in Engineering*, 2012, 89, 1069-1101.
- [30] Yue, Q., Zhou, W., Wang, Q., et al. An adaptive phase-field model based on bilinear elements for tensile-compressive-shear fracture. *Computers and Mathematics with Applications*, 2022, 105, 112-135.
- [31] Tian, F., Tang, X., Xu, T., Yang, J., Li, L. A hybrid adaptive finite element phase-field method for quasi-static and dynamic brittle fracture. *International Journal for Numerical Methods in Engineering*, 2019, 120, 1108-1125.

- [32] Krishnan, U., Gupta, A., Chowdhury, R. Adaptive phase-field modeling of brittle fracture using a robust combination of error-estimator and markers. *Engineering Fracture Mechanics*, 2022, 274, 108758.
- [33] Assaf, R., Birk, C., Natarajan, S., Gravenkamp, H. Three-dimensional phase-field modeling of brittle fracture using an adaptive octree-based scaled boundary finite element approach. *Computer Methods in Applied Mechanics and Engineering*, 2022, 399, 115364.
- [34] Shajan, A. M., Piska, R., Natarajan, S. Study of mixed-mode fracture in functionally graded material using an adaptive phase-field fracture model. *Composite*
- [35] Hirshikesh, D., Schneider, B., Nestler, B. Realization of adaptive mesh refinement for phase-field model of thermal fracture within the FEniCS framework. *Engineering Fracture Mechanics*, 2023, 293, 109676. ISSN 0013-7944.
- [36] Xu, W., Jiang, D., Zhang, C., Li, H., Qiang, S., Li, Y., Yuan, M., Zhang, C. An adaptive mesh refinement strategy for 3D phase modeling of brittle fracture. *Engineering Fracture Mechanics*, 2023, 284, 109241. ISSN 0013-7944.
- [37] Wei, H., Tian, T., Huang, Y. Fealpy: Finite element analysis library in Python. Available at: <https://github.com/weihuayi/fealpy>, Xiangtan University, 2017-2023.
- [38] Bourdin, B., Marigo, J. J., Maurini, C., Sicsic, P. Morphogenesis and propagation of complex cracks induced by thermal shocks. *Physical Review Letters*, 2014, 112, 014301.
- [39] Kobayashi, R. A brief introduction to phase field method. *AIP Conference Proceedings*, 2010, 1270(1), 282.
- [40] Wu, J. Y., Nguyen, V. P., Nguyen, C. T., Sutula, D., Sinaie, S., Bordas, S. P. A. Chapter One - Phase-field modeling of fracture. In: Bordas, S. P. A., Balint, D. S. (eds.), *Advances in Applied Mechanics*, vol. 53, Elsevier, 2020, pp. 1-183. ISSN: 0065-2156, DOI: 10.1016/bs.aams.2019.08.001.
- [41] Freddi, F., Mingazzi, L. Mesh refinement procedures for the phase field approach to brittle fracture. *Computer Methods in Applied Mechanics and Engineering*, 2022, 388, 114214. ISSN: 0045-7825, DOI: 10.1016/j.cma.2021.114214.
- [42] Freddi, F., Mingazzi, L. Adaptive mesh refinement for the phase field method: A FEniCS implementation. *Applications in Engineering Science*, 2023, 14, 100127. ISSN: 2666-4968, DOI: 10.1016/j.apples.2023.100127.
- [43] Huang, Y., Wei, H., Yang, W., Yi, N. A new a posteriori error estimate for adaptive finite element methods. In: *Domain Decomposition Methods in Science and Engineering XIX, Lecture Notes in Computational Science and Engineering*, vol. 78, Y. Huang et al. (eds.), 2011, pp. 63-74.
- [44] Huang, Y., Jiang, K., Yi, N. Some Weighted Averaging Methods for Gradient Recovery. *Advances in Applied Mathematics and Mechanics*, 2012, 4(2), 131-155. DOI: 10.4208/aamm.10-m1188.
- [45] Zhang, Z., Naga, A. A New Finite Element Gradient Recovery Method: Superconvergence Property. *SIAM J. Scientific Computing*, 2005, 26(4), 1192-1213.
- [46] Liu, H., Sun, J. Recovery type a posteriori estimates and superconvergence for nonconforming FEM of eigenvalue problems. *Applied Mathematical Modelling*, 2009, 33(8), 3488-3497. ISSN: 0307-904X, DOI: 10.1016/j.apm.2008.11.011.
- [47] Hu, J., Zhang, Z. A conforming discontinuous Galerkin finite element method. *Mathematics of Computation*, 2015, 84(292), 765-785.
- [48] Zhang, Z., Hu, J. Conforming DG methods for linear elasticity with strong symmetric stresses. *Journal of Scientific Computing*, 2016, 68(3), 1301-1328.
- [49] Zhu, Q., Steigmann, D. J. Phase-field models for fracture with higher-order gradient damage laws. *Proceedings of the Royal Society A: Mathematical, Physical and Engineering Sciences*, 2016, 472(2191), 20160615.
- [50] Borden, M. J., Hughes, T. J. R., Landis, C. M., Anvari, A., Lee, I. J. A higher-order phase-field model for brittle fracture: Formulation and analysis within the isogeometric analysis framework. *Computer Methods in Applied Mechanics and Engineering*, 2016, 312, 130-166.
- [51] Zienkiewicz, O. C., Zhu, J. Z. The superconvergent patch recovery and a posteriori error estimates. Part 1: The recovery technique. *International Journal for Numerical Methods in Engineering*, 1992, 33(7), 1331-1364.
- [52] Zhu, J. Z., Zienkiewicz, O. C. The superconvergent patch recovery and a posteriori error estimates. Part 2: Error estimates and adaptivity. *International Journal for Numerical Methods in Engineering*, 1992, 33(7), 1365-1382.
- [53] Ainsworth, M., Oden, J. T. *A posteriori error estimation in finite element analysis*. John Wiley & Sons, 2000.
- [54] Dai, X., Zhang, Z. Convergence of an adaptive finite element method for a class of non-linear evolution equations. *SIAM Journal on Numerical Analysis*, 2004, 42(2), 681-708.
- [55] CuPy. CuPy: A NumPy-like library for GPU-accelerated computing. Available at: <https://cupy.dev/>.

- [56] NumPy. NumPy: The fundamental package for scientific computing with Python. Available at: <https://numpy.org/>.
- [57] SciPy. SciPy: Open source scientific computing in Python. Available at: <https://www.scipy.org/>.
- [58] Hunter, J. D. Matplotlib: A 2D graphics environment. *Computing in Science & Engineering*, 2007, 9(3), 90-95. DOI: 10.1109/MCSE.2007.55.